coatings

Article

Microstructure and Wear Resistance of a Cr_7C_3 Reinforced Ni_3Al Composite Coating Prepared by Laser Cladding

Zhenbo Liu [1,2], Fuxing Yin [1,*], Cuixin Chen [1], Lin Zhao [2,*], Lihua Fu [3], Yingkai Feng [4], Yang Cao [2], Yun Peng [2], Zhiling Tian [2] and Changhai Li [2]

[1] School of Materials Science and Engineering, Hebei University of Technology, Tianjin 300130, China; lzbzzhy@163.com (Z.L.); karenccx@126.com (C.C.)
[2] Welding Institute, Central Iron and Steel Research Institute, Beijing 100081, China; caoyang0531@163.com (Y.C.); pengyun@cisri.com.cn (Y.P.); tianzhl@cisri.com.cn (Z.T.); changhai_bg@126.com (C.L.)
[3] National United Engineering Laboratory for Advanced Bearing Tribology, Henan University of Science and Technology, Luoyang 471003, China; flhustb@haust.edu.cn
[4] Department of Mechanical Engineering, Tsinghua University, Beijing 100084, China; fyk19@mails.tsinghua.edu.cn
* Correspondence: yinfuxing@hebut.edu.cn (F.Y.); hhnds@aliyun.com (L.Z.); Tel.: +86-10-62182946 (L.Z.)

Abstract: Using Cr_7C_3/Ni_3Al alloyed powder and Cr_3C_2/Ni_3Al mixed powder, laser cladding was carried out to prepare a Cr_7C_3 reinforced Ni_3Al composite cladding layer. The microstructure and tribological properties of the cladding materials were investigated by X-ray diffraction (XRD), scanning electron microscopy (SEM), energy dispersive spectroscopy (EDS), transmission electron microscopy (TEM), and wear tests. The results indicate that the microstructure of the Cr_7C_3/Ni_3Al alloyed powder cladding layer contains mainly Ni_3Al, NiAl, and in situ-formed Cr_7C_3, whereas Cr_3C_2 occurs in the Cr_3C_2/Ni_3Al mixed powder cladding layer. The friction coefficient and wear loss of the alloyed powder cladding layer are about 0.1 and 0.75 mg, respectively, which are less than those of the mixed powder cladding layer (0.12 and 0.8 mg). Moreover, the alloyed powder cladding layer is much friendlier to its counterpart. The counterpart's loss weight of the alloyed powder cladding layer decreases 42.2% than the mixed powder cladding layer. The reason can be attributed to the homogeneous distribution of fine in situ-formed Cr_7C_3 in the alloyed powder cladding materials, which can effectively separate the friction pair, improving the wear resistance of the cladding materials.

Keywords: laser cladding; in situ-formed Cr_7C_3; microstructure; wear resistance

check for updates

Citation: Liu, Z.; Yin, F.; Chen, C.; Zhao, L.; Fu, L.; Feng, Y.; Cao, Y.; Peng, Y.; Tian, Z.; Li, C. Microstructure and Wear Resistance of a Cr_7C_3 Reinforced Ni_3Al Composite Coating Prepared by Laser Cladding. *Coatings* **2022**, *12*, 105. https://doi.org/10.3390/coatings12010105

Received: 2 December 2021
Accepted: 13 January 2022
Published: 17 January 2022

1. Introduction

As one of the intermetallic compounds, Ni_3Al has many excellent characteristics, such as low density, a high melting point, high temperature oxidation resistance, excellent creep resistance, and outstanding high temperature wear resistance [1–4]. Furthermore, it has a special abnormal phenomenon, where its yield strength increases with temperature due to its long-range ordered crystal structure of $L1_2$ type. Therefore, the Ni_3Al alloy is expected to be applicable as a high-temperature wear-resistant material [5,6].

However, the wear resistance of monolithic Ni_3Al intermetallic compounds is usually inadequate under the most extreme conditions of severe sliding, impact wear, and abrasive wear [7,8]. Early studies have shown that the high temperature strength and hardness of Ni_3Al alloy can be significantly increased by adding Cr_3C_2 particles, which have the advantages of high hardness, high-temperature stability, excellent high-temperature wear resistance, high compatibility, and wettability with the Ni_3Al matrix [9–12]. Fu et al. [13] prepared a Cr_3C_2/Ni_3Al composite material using hot isostatic pressing technology, and studied the influence of different chromium carbide contents on the wear resistance of the composite. It was found that a certain content of chromium carbide can effectively improve the wear resistance of the material. Gong et al. [14] compared the wear resistance of the Cr_3C_2/Ni_3Al composite material with the monolithic Ni_3Al alloy and the gray cast iron, and found that the wear resistance of the composite material is far better than that of single-phase Ni_3Al alloy and the gray cast iron. Additionally, it was also found that the wear resistance of the composite material prepared by laser cladding process is superior to that of materials prepared via other preparation processes. Luo et al. [15] compared the wear resistance of Cr_3C_2/Ni_3Al composite coating and the Stellite 12 alloy at room temperature. The results revealed that the wear resistance of the Cr_3C_2/Ni_3Al composite coating is much higher than that of the Stellite 12 alloy, mainly due to the presence of a uniformly distributed hard phase on a highly work-hardened intermetallic matrix in the composite coating. In general, chromium carbide are promising candidates for further improving the tribological properties of Ni_3Al alloy [16].

Laser cladding is a complex process combining physics, chemistry, and metallurgy [17,18]. Laser irradiation causes the cladding powders to melt and solidify rapidly on the matrix surface. It forms a fine-grained and tough coating on the substrate surface, and the coating has a dense structure and good metallurgy bonding with the substrate materials [19,20]. Compared with other surface strengthening technologies, laser cladding is an efficient and clean surface modification technology [21].

However, there are only a few reports Cr_3C_2/Ni_3Al composites prepared by laser cladding. In one example, Chen et al. [22] prepared a Cr_3C_2/Ni_3Al composite coating by laser cladding, and studied the microstructure and wear resistance of the coating. The Cr_3C_2/Ni_3Al composite coating thus prepared was found to have good wear resistance. However, the distribution of the reinforcing phase was not uniform in the cladding layer prepared from mixed powders of Ni_3Al and Cr_3C_2. This will greatly influence the wear resistance of the cladding layer. Therefore, in this study, we sought to optimize the distribution uniformity of the strengthening phase in the cladding layer, via a new type of design based on the use of alloyed powders, and the alloyed powders were prepared using vacuum melting gas atomization technology. The microstructure and properties of the Cr_7C_3/Ni_3Al alloyed powder cladding layer and the Cr_3C_2/Ni_3Al mixed powder cladding layer prepared by the same process were then studied.

2. Experimental Materials and Methods

2.1. Composite Powders

Previous studies have shown that addition of about 0.02 wt.% boron plays an important role in increasing the toughness of Ni_3Al intermetallic compounds [23]. Additionally, the ratio of Cr and C should be strictly controlled because the Cr atoms will only partly be dissolved into the Ni_3Al in the smelting process, so it is necessary to ensure that the actual amount of added Cr is slightly higher than the target amount to be finally dissolved. At the same time, according to the Ni-Al phase diagram in Figure 1, only when the Al content is less than 25 at.% will the Ni_3Al be more easily generated [24,25]. Aluminum blocks, chromium blocks, nickel powders, carbon powders, and boron powders (CISRI, Beijing, China), applied as raw materials for powder atomization, were melted in a vacuum furnace at 1900~2000 °C for 1 h, and then atomized into powder. In addition, the atomization pressure also has important effects on powder morphology, fluidity and particle size distribution. Higher atomization pressure leads to a fine powder particle size, which is not suitable for laser cladding; lower atomization pressure will lead to poor sphericity of the cladding powder, which is not conducive to attaining powder with reasonable fluidity. Therefore, the atomization pressure of 2.9–3.2 MPa was selected for powder preparation [26].

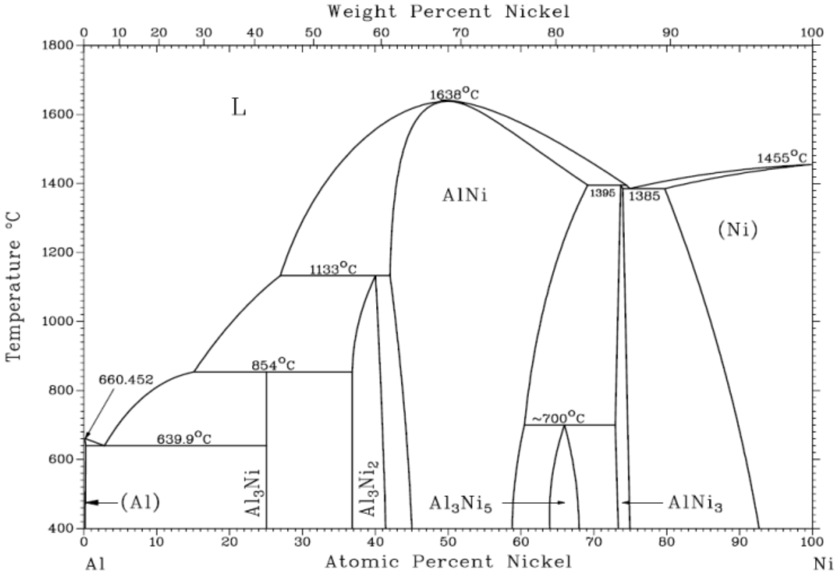

Figure 1. NiAl phase diagram.

2.2. Preparation of Cladding Layer

42CrMo alloyed steel was used as the substrate material. The Cr_7C_3/Ni_3Al alloyed powder (denoted as the alloyed powder) was prepared using the vacuum melting gas atomization technique. For comparison, the Cr_3C_2/Ni_3Al mixed powder (denoted as the mixed powder) was produced by mechanically mixing 25 wt.% Cr_3C_2 powder (CISRI, Beijing, China) and 75 wt.% Ni_3Al powder (The Chalmers University of Technology, Göteborg, Sweden) in this work. The compositions of the substrate material, alloyed powder, and mixed powder are given in Table 1. The particle size of the laser cladding powders was in a range of 45~125 µm. The laser cladding equipment used a YLS-6000 fiber laser (IPG Photonic, Oxford, MA, USA) with a rectangular spot of 5 mm × 2 mm and a focal length of 300 mm. The applied powders were fully dried at 100 °C for 30 min. Then, 400 # SiC sandpaper was used to polish the surface of the 42CrMo alloy steel. Grease and other harmful substances on the surface of the 42CrMo alloy steel pieces were removed by acetone. In the laser cladding process, we used laser coaxial-powder feeding technology, with a laser power of 2.0 kW. Other process parameters were set as follows: scanning speed, 0.18 m/min; DPSF-2 semi-automatic powder feeding device, powder feeding capacity, 1.05 kg/h; argon (purity > 99.9%), as a powder carrier, with a flow rate of protective gas of 15 L/min and a flow rate of powder gas of 5 L/min.

Table 1. 42CrMo alloy steel and powders chemical composition (wt.%).

Materials/Elements	C	Si	Mn	Cr	Mo	P	S	Fe	Ti	Ni	Al	B
42CrMo	0.43	0.25	0.56	1	0.22	0.003	0.014	Bal.	/	/	/	/
Alloyed powders	2.42	/	/	24.51	/	/	/	/	/	Bal.	9.62	0.02
Ni_3Al powders	/	/	0.78	/	/	/	/	11.61	0.56	Bal.	9.52	0.02

2.3. Microstructure Characterization and Wear Test

Phase analysis of alloyed powder and cladding layer was carried out using a Bruker D8 ADVANCE X-ray diffractometer (XRD, BRUKER, Karlsruhe, Germany) with a scanning speed of 2°/min. The microstructure and phase composition of the cladding layers were analyzed using Zeiss high-resolution field emission scanning electron microscopy (SEM, ZEISS, Jena, Germany), energy dispersive spectroscopy (EDS, ZEISS, Jena, Germany), and high-resolution transmission electron microscopy (JEM-2010, JEOL, Tokyo, Japan). The hardness distribution from the top of the cladding layer to the substrate material was measured with an FM300 microhardness tester (F-T, Tokyo, Japan). A testing load of 100 g was selected, the load retention time was l0 s, and the spacing was 100 μm. Five points were randomly selected on the cladding layer to calculate the average microhardness. A multifunctional friction and wear testing machine (UMT, BRUKER, Madison, MA, USA) was used to test the friction and wear performance. Vermicular graphite cast iron was chosen as the comparison material due to its excellent tribological properties. In the wear test, a cladding sample in the form of a pin with a size of Ø3 mm was used. Gray cast iron was used as a disk material because it has been often used as a counterpart of the piston ring components in engines, as cylinder lines, and as other high-temperature wear parts. The size of the disk was Ø24 mm [27]. Friction and wear test conditions were as follows: dry friction and wear, load of 30 N, rotation speed of 200 r/min, rotation radius of 7 mm, testing time of 60 min, and room temperature. In order to ensure the accuracy of the experimental data, the pin and disk were cleaned by exposure to ultrasonic waves in acetone before and after the test. Then, the weights before and after the wear (m1 and m2, respectively) were valued using a high-precision analytical balance. The wearing quantity $\Delta m = m1 - m2$. Thereafter, the counterpart disk was scanned by a 3D white light interferometer. The morphology of the worn surface was observed using a high-resolution field emission scanning electron microscope (Zeiss).

3. Results

3.1. Micro-Analysis on Alloyed Powders

In the process of coaxial powder feeding laser cladding, the powder properties, such as powder fluidity, morphology, and particle size distribution, have an important influence on the quality and performance of the cladding layer [28]. Therefore, the properties of the alloyed powder were first investigated. Figure 2 shows a relatively high sphericity of the alloyed powder shown by scanning electron microscopy. In addition, the morphology of the powders was statistically analyzed via scanning electron microscopy. The results indicate that the sphericity of the composite powders reached 94.2%. The particle size of the composite powder was tested by measured by laser particle size testing, and the results are shown in Figure 3. It can be seen that the particles are mostly distributed in a size range of 45~125 μm. The D50 values are also relatively uniform at about 78.413 μm, following a normal distribution. Particle size obviously affects the convergence point of powder flow and the focal length. The concentration of the convergence point under the same focal length will be higher if the powder is more concentrated, which will in turn increase its utilization rate.

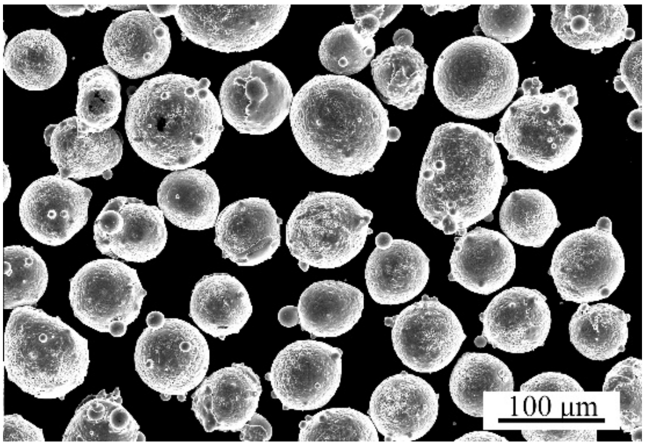

Figure 2. Morphology of the alloyed powder (SEM).

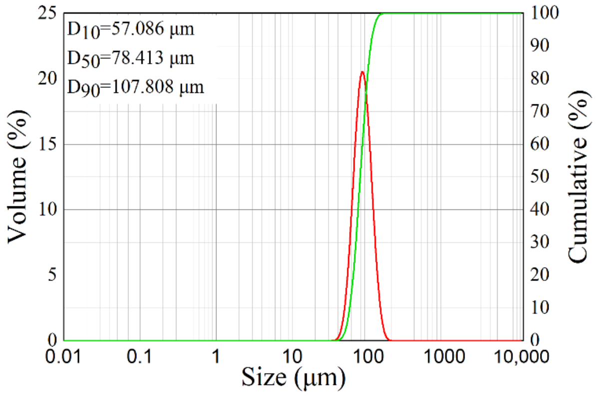

Figure 3. Particle size distribution of the alloyed powder.

The cross section morphology and microstructure of the in situ-formed alloyed powder is shown in Figure 4. It can be seen form Figure 4a that the section morphology of the powder is well distributed, and the black phase is evenly distributed on the gray matrix. Figure 4b shows a backscattering electron image of the alloyed powders, and there are three different color areas, marked as P1, P2, and P3. In the process of powder preparation, Cr element will diffuse into the Ni_3Al crystal structure, partially replacing both the Ni and Al elements, resulting in NiAl phase formation [29]. The XRD pattern of the alloyed powders, shown in Figure 5, reveal that there are three phases of Ni_3Al, NiAl, and Cr_7C_3 in the powder. At the same time, the diffraction peaks of Ni_3Al shift due to a lattice spacing change. When Cr enters the crystal structure of Ni_3Al, it has a better affinity with the Al element, so it will preferentially occupy the position of Al, resulting in an increase to the crystal plane spacing. Therefore, it can be concluded that P1 is the NiAl phase, P2 is the Ni_3Al phase, and P3 is Cr_7C_3 the phase.

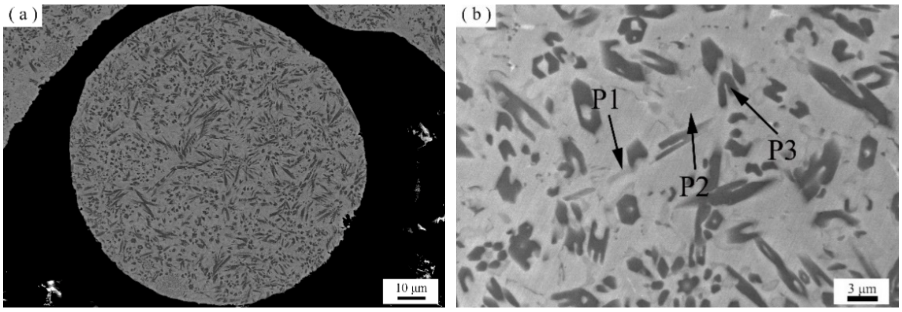

Figure 4. Cross section morphology (**a**) and microstructure (**b**) of the alloyed powder.

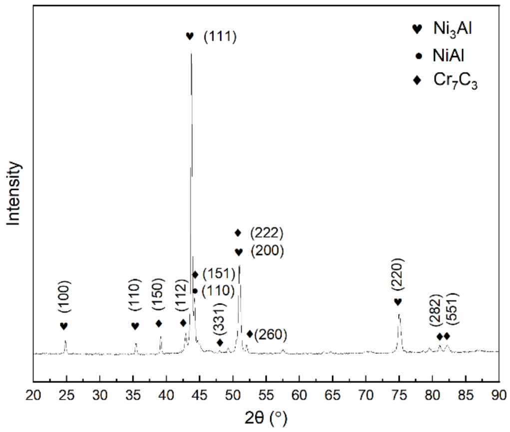

Figure 5. XRD spectrum of the alloyed powder.

3.2. Microstructure and Phase Composition of Cladding Layer

Figure 6a,b shows the section morphology of the alloyed powder cladding layer and the mixed powder cladding layer, respectively. The cladding layer structures are relatively dense and uniform. Moreover, the wetting angle of the cladding layer is relatively large, which is conducive to multi-lap bonding. The fast laser cladding process led the solidification rate of molten pool being higher than the rate of bubble escape, resulting in the formation of micropores [30]. In addition, it can be seen that the substrate material was partially re-melted, which suggest that strong metallurgical bonding was created between the cladding layer and the substrate. Figure 6c,e shows a similar local microstructure in the alloyed powder cladding layer, a uniform distribution of the phase constitution, and regular patterns. Figure 6d,f shows different morphology from the mixed powder cladding layer. It can be seen that the morphology, size, and distribution of carbides in the two areas are different and less regular. It may be concluded that the size of particles in the black strengthening phase in the cladding layer prepared by the alloyed powders is consistent, with more uniform and regular distribution.

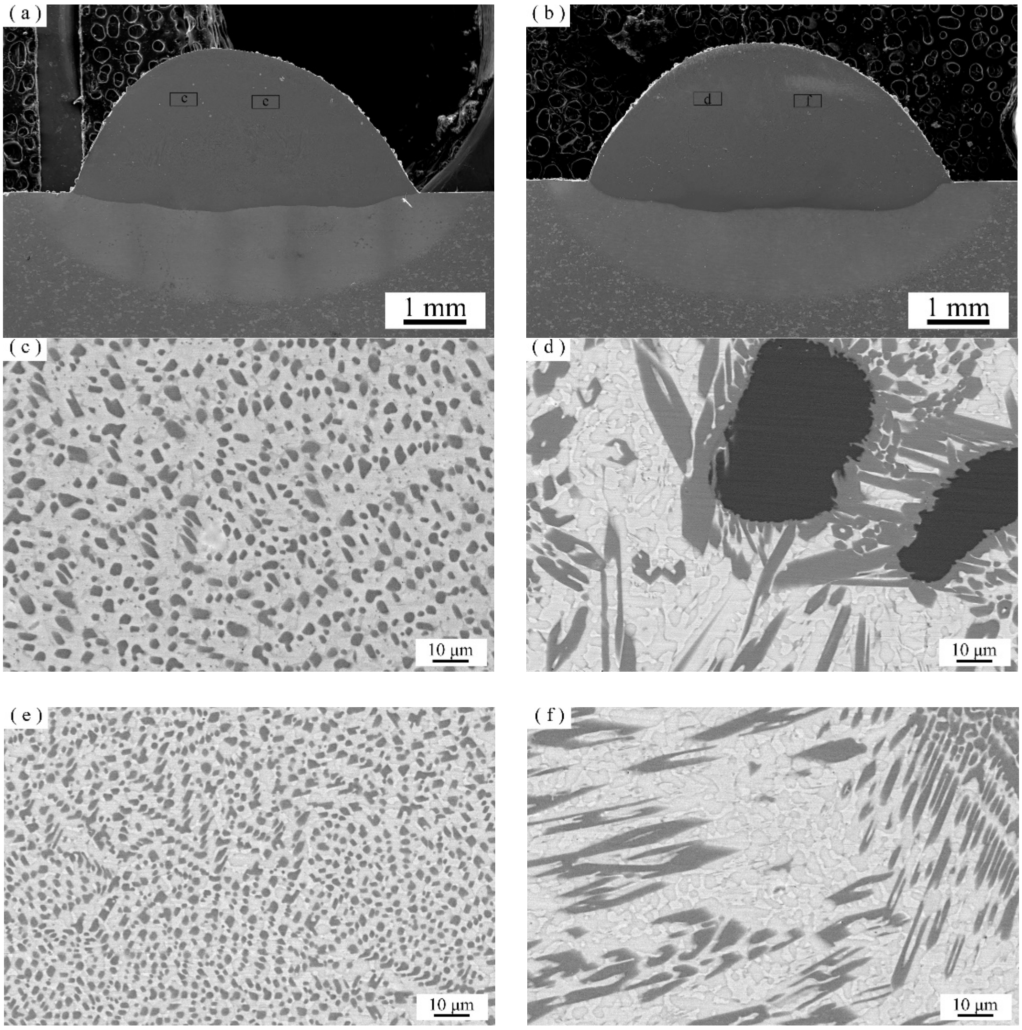

Figure 6. Macrostructure and microstructure morphologies of cladding layer cross section. (**a**,**c**,**e**) from the alloyed powder cladding layer; (**b**,**d**,**f**) from the mixed powder cladding layer.

Figure 7 shows that the alloyed powder cladding layer is mainly composed of Ni_3Al, Cr_7C_3 and NiAl phases. Additionally, the mixed powder cladding layer is varied, being composed of Ni_3Al, Cr_7C_3, Cr_3C_2 and NiAl phases. In theory, chromium carbide may exist in three forms, Cr_3C_2, Cr_7C_3 and $Cr_{23}C_6$, and their Gibbs energy is [31] calculated respectively as:

$$\Delta G_f^0(Cr_3C_2) = -54,344 - 19.57\ T(\pm 9400)\ J/mol \quad (1)$$

$$\Delta G_f^0(Cr_7C_3) = -92,067 - 41.5\ T(\pm 2800)\ J/mol \quad (2)$$

$$\Delta G_f^0(Cr_{23}C_6) = -236,331 - 86.2\ T(\pm 10,000)\ J/mol \quad (3)$$

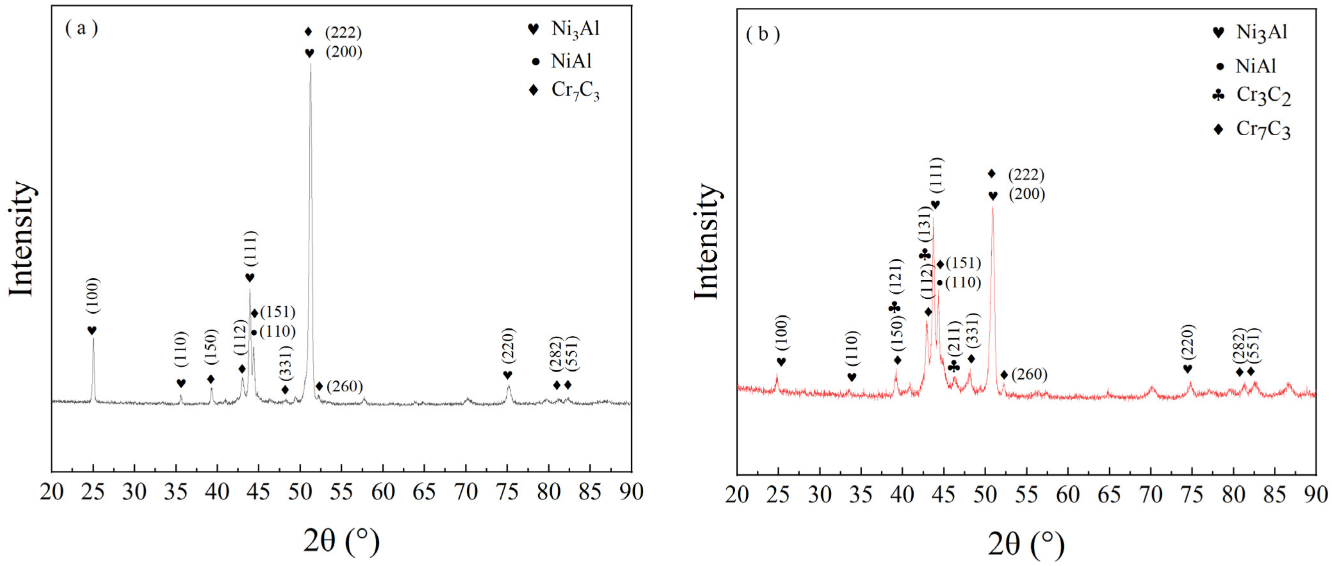

Figure 7. XRD spectra of the two cladding layers: (**a**) the alloyed powder cladding layer; (**b**) the mixed powders cladding layer.

At the same temperature, the Gibbs energy of the three kinds of chromium carbide is $Cr_3C_2 > Cr_7C_3 > Cr_{23}C_6$. The smaller the Gibbs free energy, the more stable it is. However, studies have shown that the most thermodynamically stable $Cr_{23}C_6$ can be formed only in the case of long-term heat treatment, while the materials in the laser cladding state are all in a non-equilibrium stage of solidification. Considering the Cr/C ratio in the powders, the phase in the alloyed powder cladding layer is excepted to comprise Cr_7C_3 [32]. EDS mapping of the alloyed powder cladding layer is shown in Figure 8. Considering the result of EDS mapping together with XRD analysis data, it can be determined that the black Cr and C elements containing rich phases could be a strengthening phase of Cr_7C_3. The gray area and the white area are rich in both Ni and Al, with small amounts of Cr and C. It should also be noted that the positions of the Ni_3Al and NiAl diffraction peaks of the cladding layer are offset compared to those of standard PDF cards. This is because the Cr and C elements enter the Ni_3Al and NiAl crystal structures and replace the occupied positions of Ni or Al, which caused lattice distortion and spacing change. The Al element content of the gray areas differs, with the dark gray area determined as NiAl and the white gray area as Ni_3Al. The rapid thermal process of laser cladding leads to non-equilibrium state of liquid solidification and, thus, an unequilibrium NiAl phase was formed. The NiAl phase may strengthen the Ni_3Al matrix [33]. The residual coarse Cr_3C_2 in the mixed powder cladding layer is due to the large particle size of Cr_3C_2 in the mixed powder cladding layer, which only partially dissolves in the cladding layer [34].

Figure 9 shows TEM images and selected electron diffraction patterns of the alloyed powder cladding layer. There are three phases in the TEM images of the alloy powder cladding layer shown in Figure 9a. Figure 9b shows the electron diffraction pattern of the Ni_3Al fcc structure. Figure 9c shows the electron diffraction pattern of the NiAl bcc structure. Figure 9d shows the electron diffraction pattern of the Cr_7C_3 hcp structure. Figure 10 shows the TEM image and the selected electron diffraction pattern of the alloyed powder cladding layer. Figure 10a–e shows TEM images of the Ni_3Al, NiAl, Cr_7C_3, and

Cr_3C_2 phases, respectively. Figure 10b shows the electron diffraction pattern of the Ni_3Al fcc structure; Figure 10c shows the electron diffraction pattern of the NiAl bcc structure; and Figure 10d shows the electron diffraction pattern of the Cr_7C_3 hcp structure. The electron diffraction pattern of the Cr_3C_2 bcc structure is shown in Figure 10f.

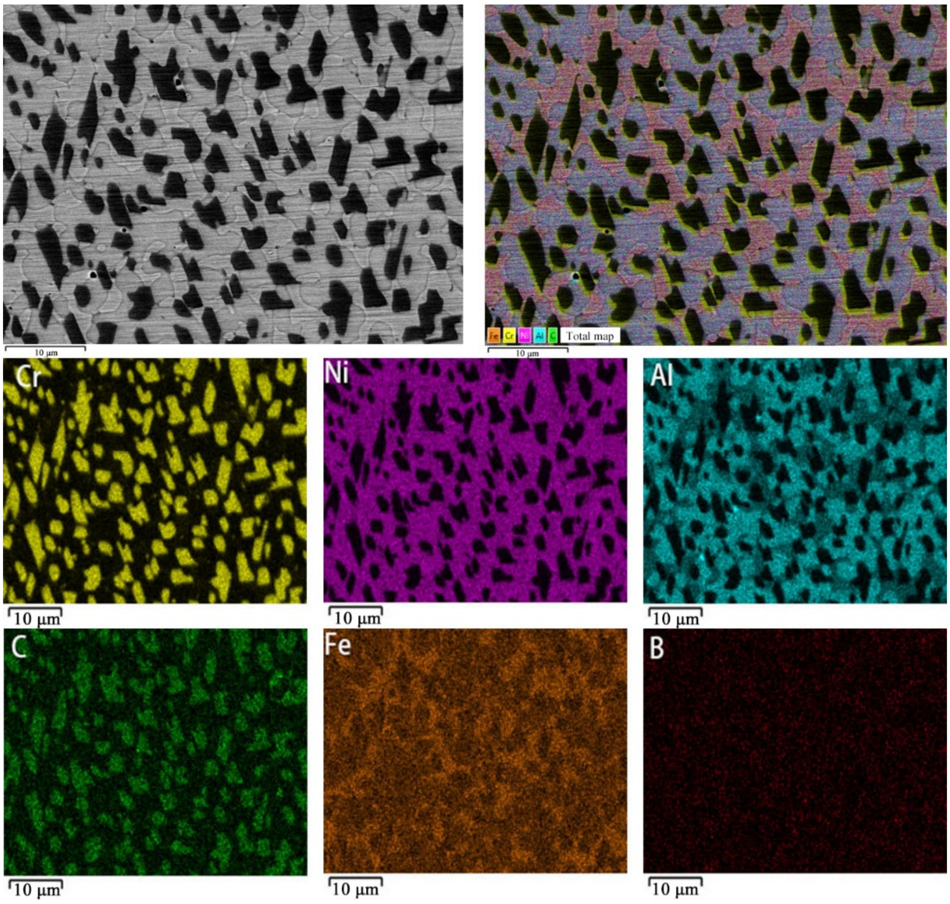

Figure 8. Element distribution map of the alloyed powder cladding layer.

As mentioned above, there is are obvious differences in microstructure between the images represented in Figure 6c,e and those in Figure 6d,f. The mixed powder cladding layers are composed of four phases, consisting of a matrix of Ni_3Al, NiAl, Cr_7C_3, and the partially dissolved Cr_3C_2, revealed by XRD and TEM analyses; see Figure 6d,f. Some of the coarse Cr_3C_2 particles and the Cr_7C_3 particles in the mixed powder cladding layer are bulky and uneven. The mixed powders were mixed by mechanical stirring of Ni_3Al and Cr_3C_2. The difference in shape and density between Ni_3Al and Cr_3C_2 leads to a difference in carrying capacity during the coaxial powder feeding process, resulting in an uneven distribution of Cr_3C_2 in the mixed powder entering the molten pool. Since the laser cladding process is very rapid, the Cr_3C_2 particles have no time to fully dissolve and diffuse in molten pool, resulting in the uneven distribution of Cr_7C_3 particles. Additionally, some of the coarse Cr_3C_2 particles were retained due to their higher melting point and the shorter time of the laser cladding process. The alloyed powder cladding layer is composed of a matrix of Ni_3Al and two other phases, NiAl + Cr_7C_3 (black). The Cr_7C_3 particles in the alloyed powder cladding layer are tiny and equally distributed; see Figure 6c,e. Because the Cr_7C_3 particles are relatively small and evenly distributed in each alloyed powder, in situ-formed Cr_7C_3 shows uniform and even dispersion without element diffusion in the process of laser cladding.

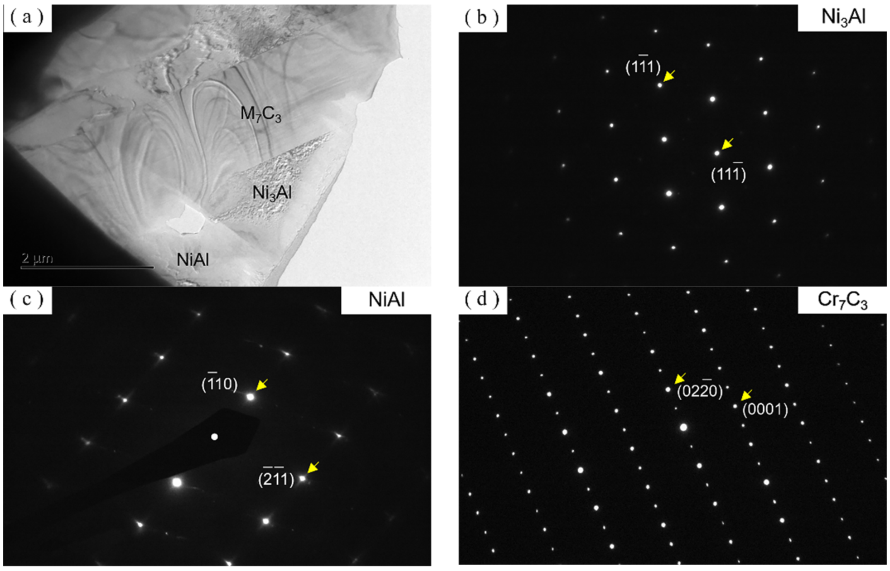

Figure 9. TEM results of the alloyed powder cladding layer. (**a**) TEM image of Ni_3Al, NiAl, and Cr_7C_3; (**b**–**d**) electron diffraction patterns of Ni_3Al, NiAl, and Cr_7C_3, respectively.

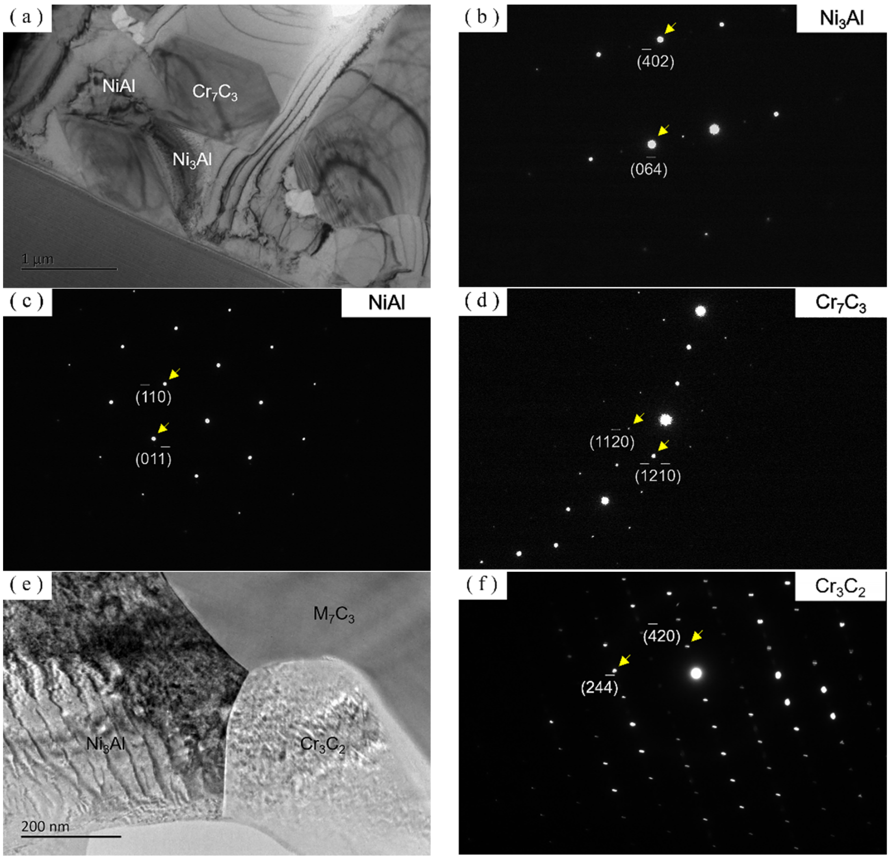

Figure 10. TEM results of the mixed powder cladding layer. (**a**,**e**) TEM images of Ni_3Al, NiAl, Cr_7C_3, and Cr_3C_2; (**b**–**d**) electron diffraction patterns of Ni_3Al, NiAl, and Cr_7C_3 respectively; (**f**) electron diffraction pattern of Cr_3C_2.

3.3. Microhardness and Wear Properties of the Cladding Layer

Figure 11 shows the change of microhardness from the surface to the substrate of the cladding layer. It can be seen that the two cladding layers have the same hardness variation trend. The average microhardness of the alloyed powder cladding layer is 600 ± 5 $HV_{0.1}$, and remains constant. However, the average microhardness of the mixed powder cladding layer is about 550 ± 5 $HV_{0.1}$, and the fluctuation range of the hardness value is relatively large. The varied microhardness of the cladding layer is related to its microstructure. In fact, the tiny Cr_7C_3 strengthening phase is uniformly distributed on the Ni_3Al matrix in the alloyed powder cladding layer, whereas the distribution of Cr_7C_3 and Cr_3C_2 in the mixed powder cladding layer is not uniform. The thickness of the cladding layer is 2.25 ± 0.1 mm. The average microhardness of the 42CrMo matrix is about 270 ± 5 $HV_{0.1}$, and the hardness of the cladding layer is more than one-fold higher than that of the substrate materials.

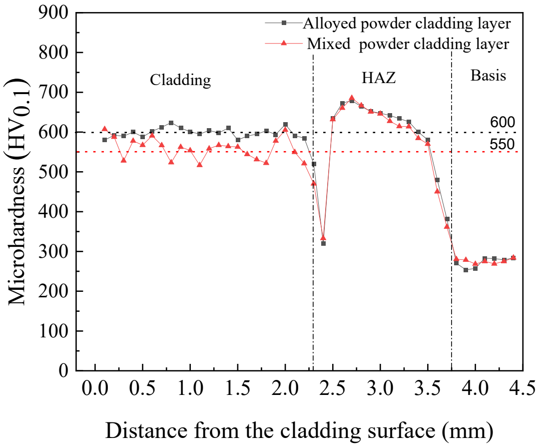

Figure 11. Microhardness of the two cladding layers.

Figure 12 shows the dynamic friction coefficient curves of three tribo-pairs at room temperature. They reveal that the coefficient of the alloyed powder cladding layer is the lowest, which is only 0.1 ± 0.01, and the coefficient of the mixed powder cladding is 0.12 ± 0.01. The friction coefficients of the alloyed powder cladding layer and the mixed powder cladding layer remain stable at a friction stage. However, a shorter time is needed for the alloyed powder cladding layer to enter the stable friction stage, and the friction coefficient is lower; the friction coefficient of vermicular cast iron is the highest, at 0.55 ± 0.05 and fluctuates greatly over time. The results indicated that compared to the mixed powder cladding layer, the alloyed powder cladding layer has an obviously reduced friction coefficient of the friction pair and displays better tribological performance.

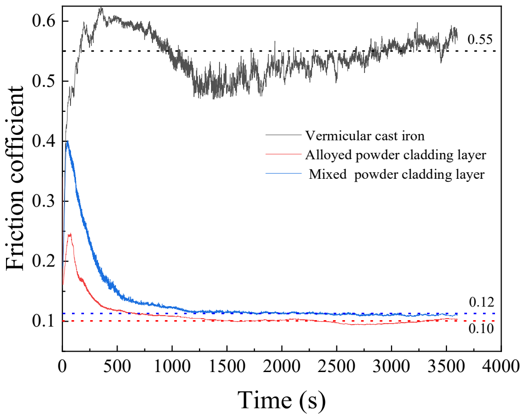

Figure 12. Friction coefficient of three tribo-pairs as a function of sliding time.

Figure 13 shows the weight loss of the three tribo-pairs above. The wear amounts of the two cladding layers are smaller, which is half that of the vermicular graphite cast iron, indicating that the addition of chromium carbide in the Ni_3Al composite for coating has greatly improved the wear resistance of the material. It should also be noted that the wear amount of the alloyed powder cladding layer is lower than that of the mixed powder cladding layer. Compared with vermicular cast iron, both of the cladding layers are more friendly to their counterparts. In fact, the counterpart's loss weight of the alloyed powder cladding layer show even better (0.82 ± 0.05 mg) than the mixed powder cladding layer (1.42 ± 0.05 mg).

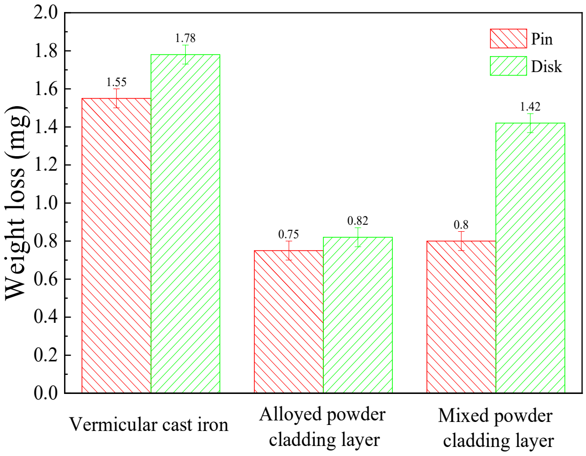

Figure 13. Weight loss of three friction pairs vs. sliding time at room temperature.

4. Discussion

Secondary electron images (SEI) and backscattering electron images (BEI) of the worn surfaces of the cladding layers are shown in Figure 14. Grooves, debris layers, and microcracks on the surface of the cladding layers are indicated. The vermicular cast iron surface has deep grooves and large debris layers, as seen in Figure 14a. The study indicated that the wear mechanisms are mainly adhesive wear and abrasive wear. There are only some small and discontinuous grooves on the surface of the cladding layer in Figure 14c,d, and the wear marks are blocked by the hard strengthening phase Cr_7C_3, which may improve the hardness and wear resistance of the material, and the wear type is abrasive wear. Figure 14e,f shows the topography of the worn surface of the mixed powder cladding layer. There are also grooves on the worn surface, but they are deeper than those on the worn surface of the alloyed powder cladding layer. The debris layers and cracks exist around the large Cr_3C_2 particles on the worn surface. The friction mechanisms are types of abrasive wear and trace adhesion wear. The wear resistance of the alloyed powder cladding layer and the mixed powder cladding layer is better than that of the vermicular graphite cast iron, mainly due to a higher work hardening ability of Ni_3Al-matrix. During the process of friction, a thickness gradient verified work hardening layer is formed on the surface of Ni_3Al material, which improves the wear resistance of the material [35]. At the same time, the raised Cr_7C_3 in the cladding layer can separate the friction surfaces well and reduce the shear force between the friction pairs, thus reducing the friction coefficient and the amount of wear [36].

The wear resistance of the alloyed powder cladding layer is better than that of the mixed powder cladding layer, which can be attributed to the following reasons: (1) The Cr_7C_3 particles in the alloyed powder cladding layer are relatively small and evenly distributed, which can more effectively separate the contact surfaces of friction pairs; the uneven distribution of Cr_7C_3 in the mixed powder cladding layer leads to a less effective separation of some contacted areas of the friction pair, and then adhesive wear is formed in these areas. (2) The Cr_7C_3 particles in the alloyed powder cladding layer are relatively small, more evenly dispersed, and held tightly by the matrix, which may effectively block and cut off local wear, and then make the debris smaller as a result. Coarse Cr_3C_2 particles exist in the cladding layer of the mixed powder, and these particles will create deep trenches on the surface of the grinding disk, even causing fatigue cracks around the larger Cr_3C_2 particles during a longer period of wear. The created bigger debris will cause more serious and intensified wear and deeper wear marks [37,38].

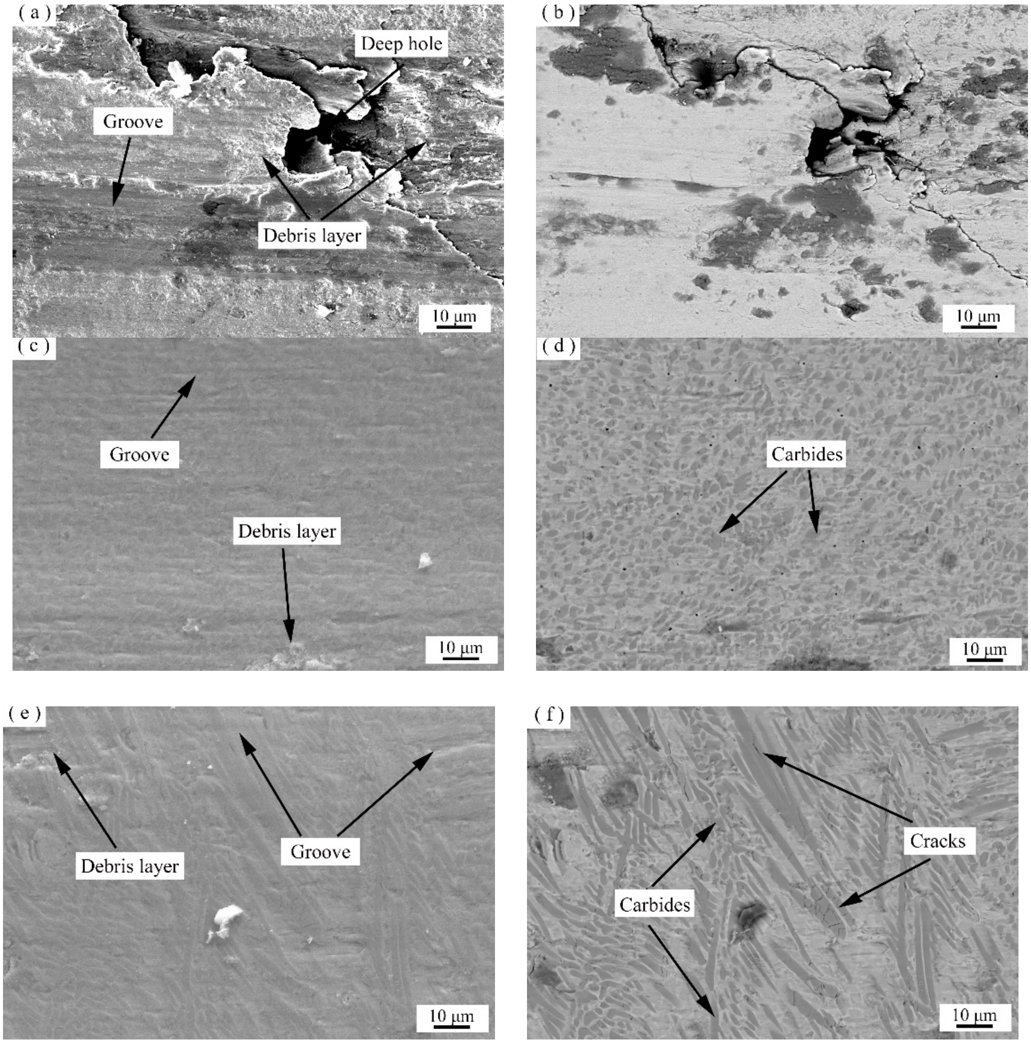

Figure 14. Secondary electron images (**a**,**c**,**e**) and backscattering electron images (**b**,**d**,**f**) of worn surfaces of vermicular cast iron, the alloyed powder cladding layer, and the mixed powder cladding layer, respectively.

The evaluation of wear performance depends not only on the low friction coefficient, wear quantity and better wear morphology of the friction material itself, but also on the wear quantity and wear morphology of its counterpart. Figure 15 shows the microstructure of the worn surfaces and 3D profile of the wear mark depth of the relative counterpart. As can be seen from the figures, the scratches on the surface of the counterpart disk against the cladding layer are relatively shallow, and only a small amount of the debris layer is on its surface. The vermicular cast iron pin made the grooves deeper, with a large debris layer on the surface of the counterpart disk. From Figure 15g, it can be seen that the wear depth on the disk related to the alloyed powder cladding layer and the mixed powder cladding layer is shallow. Additionally, the average wear depths of these disks are 18 ± 0.5, 50 ± 0.5, 70 ± 0.5 µm, corresponding to the alloyed powder cladding layer, the mixed powder cladding layer, and the vermicular cast iron, respectively. These results are consistent with the weight loss of the disk shown in Figure 13.

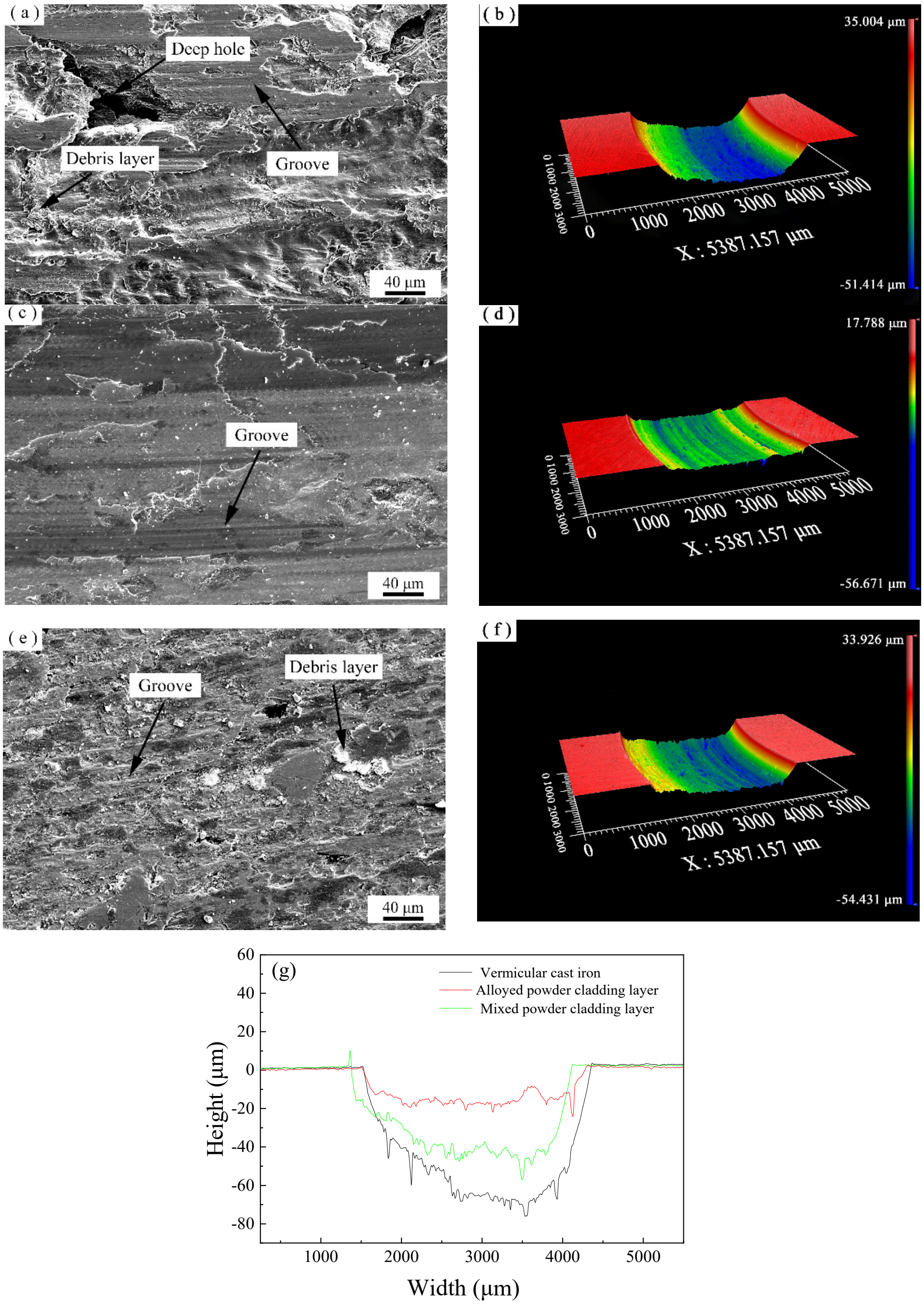

Figure 15. Worn surface morphologies and 3D profiles of counterpart disks: (**a**,**b**) vermicular cast iron; (**c**,**d**) the alloyed powder cladding layer; (**e**,**f**) the mixed powder cladding layer; (**g**) contrast diagram of wear depth on disk.

The in situ-formed Cr_7C_3 in the cladding layer can effectively separate the friction pair, and the fallen wear debris can be discharged over time to reduce the friction shear force on the surface of the grinding disk, decreasing the probability of the generation and propagation of defects, such as wear surface cracks, and reducing wear of the grinding disk [39].

5. Conclusions

(1) The alloyed powder cladding layer is mainly composed of Ni_3Al, NiAl and in situ Cr_7C_3, and the in situ-formed Cr_7C_3 particles are tiny and evenly dispersed; the mixed

powder cladding layer contains Ni_3Al, NiAl, in situ Cr_7C_3 and partially undissolved Cr_3C_2, and the distribution of the Cr_7C_3 particles is uneven.

(2) The average friction coefficient of the alloyed powder cladding layer is 0.1 ± 0.01, which is slightly lower than 0.12 ± 0.01 of the mixed powder cladding layer, and far lower than 0.55 ± 0.05 of vermicular cast iron. The wear loss of the disks related to the alloyed powder cladding layer is 0.82 ± 0.05 mg, lower than 1.42 ± 0.05 mg of the mixed powder cladding layer, and even lower compared to that of the vermicular cast iron (1.78 ± 0.05 mg).

(3) The difference in tribological performance between the alloy powder and mixed powder cladding layer is mainly due to their differences in their microstructure. In situ-formed tiny Cr_7C_3 particles are evenly dispersed on the intermetallic matrix in the alloyed powder cladding layer, which can effectively separate the friction surface and block scratches, whereas Cr_7C_3 particles generated in the mixed powder cladding layer are unevenly distributed, with inferior performance in terms of separating some surface areas of tribo-pairs. Moreover, the undissolved coarse Cr_3C_2 particles may scratch the counterpart pair more seriously and intensify the wear. Therefore, the alloyed powder cladding layer designed, produced, and tested in this study not only has improved tribological properties but also results in less damage to counterpart materials.

Author Contributions: Conceptualization, F.Y., Z.L. and C.C.; methodology, Z.L. and L.Z.; validation, F.Y., C.C. and L.Z.; formal analysis, Z.L.; investigation, Y.F. and L.F.; resources, L.Z.; data curation, Z.L. and C.C.; writing—original draft preparation, Z.L. and F.Y.; writing—review and editing, F.Y. and Z.L.; visualization, Y.F.; supervision, L.Z., Y.C., Y.P., Z.T. and C.L.; project administration, L.Z.; funding acquisition, L.Z. and L.F. All authors have read and agreed to the published version of the manuscript.

Funding: This research was funded by the National Key R&D Program of China, grant number 2020YFE0200900 and the Natural Science Foundation of Henan, grant number 202300410143.

Institutional Review Board Statement: Not applicable.

Informed Consent Statement: Not applicable.

Data Availability Statement: Not applicable.

Conflicts of Interest: The authors declare no conflict of interest.

References

1. Li, J.; Peng, Y.; Zhang, J.; Yin, S.; Ding, J.; Wu, Y.; Wu, J.; Chen, X.; Xia, X.; He, X.; et al. Cyclic oxidation behavior of Ni_3Al-based superalloyed. *Vacuum* **2019**, *169*, 108938. [CrossRef]
2. Mao, R.; Fan, Z.; Xiang, D. Enhanced mechanical properties of tungsten alloy by synergistic strengthening of flaky Ni_3Al and Al_2O_3 nano-particles. *J. Alloys Compd.* **2021**, *898*, 162790. [CrossRef]
3. Khoei, A.R.; Eshlaghi, G.T.; Shahoveisi, S. Atomistic simulation of creep deformation mechanisms in nickel-based single crystal superalloys. *Mater. Sci. Eng. A* **2021**, *809*, 14097. [CrossRef]
4. Gong, S.; Shang, Y.; Zhang, J.; Guo, X.; Lin, J.; Zhao, X. Application and research of typical intermetallics-based high temperature structural materials in China. *Acta Met. Sin* **2019**, *55*, 1067–1076. [CrossRef]
5. Wen, Y.; Sun, J.; Huang, J. First—principles study of stacking fault energies in Ni_3Al intermetallic alloyeds. *Trans. Nonferrous Met. Soc. China* **2012**, *22*, 661–664. [CrossRef]
6. Kruml, T.; Conforto, E.; Piccolo, B.L.; Caillard, D.; Martin, J.L. From dislocation cores to strength and work-hardening: A study of binary Ni_3Al. *Acta Mater.* **2002**, *50*, 5091–5101. [CrossRef]
7. Mao, Q.; Yang, Q.; Xiong, W.; LI, S.; Zhang, M.; Ruan, L. Corrosion behavior of Ni_3Al-bonded TiC-based cermets in H_2SO_4 and NaOH solutions. *Ceram. Int.* **2018**, *44*, 13303–13312. [CrossRef]
8. Li, S.; Feng, D.; Luo, H. Microstructure and abrasive wear performance of chromium carbide reinforced Ni_3Al matrix composite coating. *Surf. Coat. Technol.* **2007**, *201*, 4542–4546. [CrossRef]
9. Liu, W.; Zhang, F.; Lu, J.; Chen, J.; Huang, H.; Zhou, Y.; Tang, H. Preparation of Ni_3Al bonded diamond core drill with Ni–Cr alloyed and its performance on glass–ceramic. *Ceram. Int.* **2018**, *44*, 23080–23087. [CrossRef]
10. Colaco, R.; Vilar, R. Abrasive wear of metallic matrix reinforced materials. *Wear* **2003**, *255*, 643–650. [CrossRef]
11. Cios, G.; Bala, P.; Stepien, M.; Górecki, K. Microstructure of cast Ni-Cr-Al-C alloy. *Arch. Metall. Mater.* **2015**, *60*, 145–148. [CrossRef]

12. Gong, K.; Zhou, Z.; Shum, P.W.; Luo, H.; Tian, Z.; Li, C. Tribological evaluation on Ni_3Al-based alloyed and its composites under unlubricated wear condition. *Wear* **2011**, *270*, 195–203. [CrossRef]
13. Fu, L.; Han, W.; Gong, K.; Bengtsson, S.; Dong, C.; Zhao, L.; Tian, Z. Microstructure and tribological properties of Cr_3C_2/Ni_3Al composite materials prepared by hot isostatic pressing (HIP). *Mater. Des.* **2017**, *115*, 203–212. [CrossRef]
14. Gong, K.; Luo, H.; Feng, D.; Li, C. Wear of Ni_3Al-based materials and its chromium-carbide reinforced composites. *Wear* **2008**, *265*, 1751–1755. [CrossRef]
15. Luo, H.; Gong, K.; Li, S.; Cao, X.; Zhang, X.; Feng, D.; Li, C. Abrasive wear comparison of Cr_3C_2/Ni_3Al composite and stellite 12 alloyed cladding. *J. Iron Steel Res. Int.* **2007**, *14*, 15–20. [CrossRef]
16. Li, S.; Wu, M.; Sun, L.; Jiang, L.; Han, Y. Fretting wear resistance of ATW Cr_3C_2/Ni_3Al composite hardfacing on IC6SX. *Mater. Sci. Forum* **2010**, *654*, 532–537. [CrossRef]
17. Ma, Q.; Dong, Z.; Ren, N.; Hong, S.; Chen, J.; Hu, L.; Meng, W. Microstructure and mechanical properties of multiple in-situ-phases-reinforced nickel composite coatings deposited by wide-band laser. *Coatings* **2021**, *11*, 36. [CrossRef]
18. Sun, F.; Cai, K.; Li, X.; Pang, M. Research on laser cladding Co-based alloy on the surface of vermicular graphite cast iron. *Coatings* **2021**, *11*, 1241. [CrossRef]
19. Gao, J.; Wu, C.; Hao, Y.; Xu, X.; Guo, L. Numerical simulation and experimental investigation on three-dimensional modelling of single-track geometry and temperature evolution by laser cladding. *Opt. Laser Technol.* **2020**, *129*, 106287. [CrossRef]
20. Weisheit, A.; Rittinghaus, S.; Dutta, A.; Majumdar, J.D. Studies on the effect of composition and pre-heating on microstructure and mechanical properties of direct laser clad titanium aluminide. *Opt. Lasers Eng.* **2020**, *131*, 106041. [CrossRef]
21. Li, M.; Han, B.; Song, L.; He, Q. Enhanced surface layers by laser cladding and ion sulfurization processing towards improved wear-resistance and self-lubrication performances. *Appl. Surf. Sci.* **2020**, *503*, 144226. [CrossRef]
22. Chen, C.; Zhao, X.; Fang, Q.; Zhao, L.; Han, W.; Peng, Y.; Yin, F.; Tian, Z. Wear Resistance of Laser Cladding Ni_3Al/Cr_3C_2 Composites. *Rare Met. Mater. Eng.* **2020**, *49*, 1388–1394. (In Chinese)
23. Aoki, K.; Osamu, I. Improvement in room temperature ductility of the L12 type intermetallic compound Ni_3Al by boron addition. *J. Jpn. Inst. Met. Mater.* **1979**, . *43*, 1190–1196. [CrossRef]
24. Yuan, J.; Yu, Y.; Shen, J. Cermet composite coating with a ductile Ni_3Al binder phase and an in-situ Cr_7C_3 augmented phase. *Intermetallics* **2021**, *138*, 107300. [CrossRef]
25. Zhu, H.; Shen, J.; Gao, F.; Yu, Y.; Li, C. Microstructure and sliding wear performance of Cr_7C_3-$(Ni,Cr)_3(Al,Cr)$ coating deposited from Cr_7C_3 in situ formed atomized powder. *J. Therm. Spray Technol.* **2017**, *26*, 254–264. [CrossRef]
26. Guo, S.; Chen, Z.; Zhang, Q.; Lou, C.; Yao, J. Effects of different pressures on laser cladding special powder prepared by gas atomization. *Chin. J. Lasers* **2013**, *40*, 150–155. [CrossRef]
27. Sui, Q.; Zhou, H.; Zhang, D.; Chen, Z.; Zhang, P. Imposed thermal fatigue and postthermal-cycle wear resistance of biomimetic gray cast iron by laser treatment. *Metall. Mater. Trans. A* **2017**, *48*, 3758–3769. [CrossRef]
28. Liu, H.; Yu, G.; He, X.; Li, S. Influence of powder properties on powder flow field in coaxial Powder feeding laser cladding. *Chin. J. Lasers* **2013**, *40*, 102–110. (In Chinese)
29. Li, Y.; Li, C.; Yu, L.; Ma, Z.; Li, H.; Liu, Y. Characterization of γ' precipitate and γ/γ' interface in polycrystalline Ni_3Al-based superalloys. *Vacuum* **2020**, *176*, 109310. [CrossRef]
30. Zhang, T.; Sun, R. Study on pores and crack sensitivity of Ni- based composite coating by laser cladding. *IOP Conf.Ser. Mater. Sci. Eng.* **2015**, *87*, 012096. [CrossRef]
31. Anthonysamy, S.; Ananthasivan, K.; Kaliappan, I.; Chandramouli, V.; Rao, P.R.V.; Mathews, C.K.; Jacob, K.T. Gibbs energies of formation of chromium carbides. *Metall. Mater. Trans. A* **1996**, *27*, 1919–1924. [CrossRef]
32. Tiegs, T.N.; Alexander, K.B.; Plucknett, K.P.; Menchhofer, P.A.; Becher, P.F.; Waters, S.B. Ceramic composites with a ductile Ni_3Al binder phase. *Mater. Sci. Eng. A* **1996**, *209*, 243–247. [CrossRef]
33. Gong, K.; An, T.; Zhou, Z.; Tian, Z.; Li, C. Study on Wear Behaviors of Ni_3Al/Cr-Carbides Cladding Layer on High Strength Steel Substrate. *Adv. Mater. Res.* **2014**, *936*, 1273–1282. [CrossRef]
34. Vlasyuk, R.Z.; Radomysel'skii, I.D.; Smirnov, V.P.; Sotnik, A.A. Dissolution of Cr_3C_2 in a Nickel matrix during sintering I. Reaction of chromium carbide with nickel during solid-phase sintering. *Powder Metall. Met. Ceram.* **1985**, *24*, 269–273. [CrossRef]
35. Fu, L.; Han, W.; Zhao, L.; Gong, K.; Bengtsson, S.; Zhou, M.; Li, C.; Tian, Z. Effects of Cr_3C_2 content and temperature on sliding friction and wear behaviors of Cr_3C_2/Ni_3Al composite materials. *Wear* **2018**, *414–415*, 163–173. [CrossRef]
36. Zhai, W.; Shi, X.; Wang, M.; Xu, Z. Grain refinement: A mechanism for graphene nanoplatelets to reduce friction and wear of Ni_3Al matrix self-lubricating composites. *Wear* **2014**, *310*, 33–40. [CrossRef]
37. Yuan, Y.; Li, Z. Effects of rod carbide size, content, loading and sliding distance on the friction and wear behaviors of $(Cr,Fe)_7C_3$-reinforced α-Fe based composite coating produced via PTA welding process. *Surf. Coat. Technol.* **2014**, *248*, 9–22. [CrossRef]
38. Hu, J.; Li, D.; Llewellyn, R. Computational investigation of microstructural effects on abrasive wear of composite materials. *Wear* **2005**, *259*, 6–17. [CrossRef]
39. Wesmann, J.A.R.; Espallargas, N. Effect of atmosphere, temperature and carbide size on the sliding friction of self-mated HVOF WC–CoCr contacts. *Tribol. Int.* **2016**, *101*, 301–313. [CrossRef]